

-Supplementary Information-

On How Experimental Conditions Affect the Electrochemical Response of Disordered Nickel Oxyhydroxide Films

Rodney D. L. Smith, Rebecca S. Sherbo, Kevan E. Dettelbach and Curtis P. Berlinguette*

*Departments of Chemistry and Chemical & Biological Engineering, The University of British Columbia,
2036 Main Mall, Vancouver, BC V6T1Z1, Canada*

Correspondence to: cberling@chem.ubc.ca

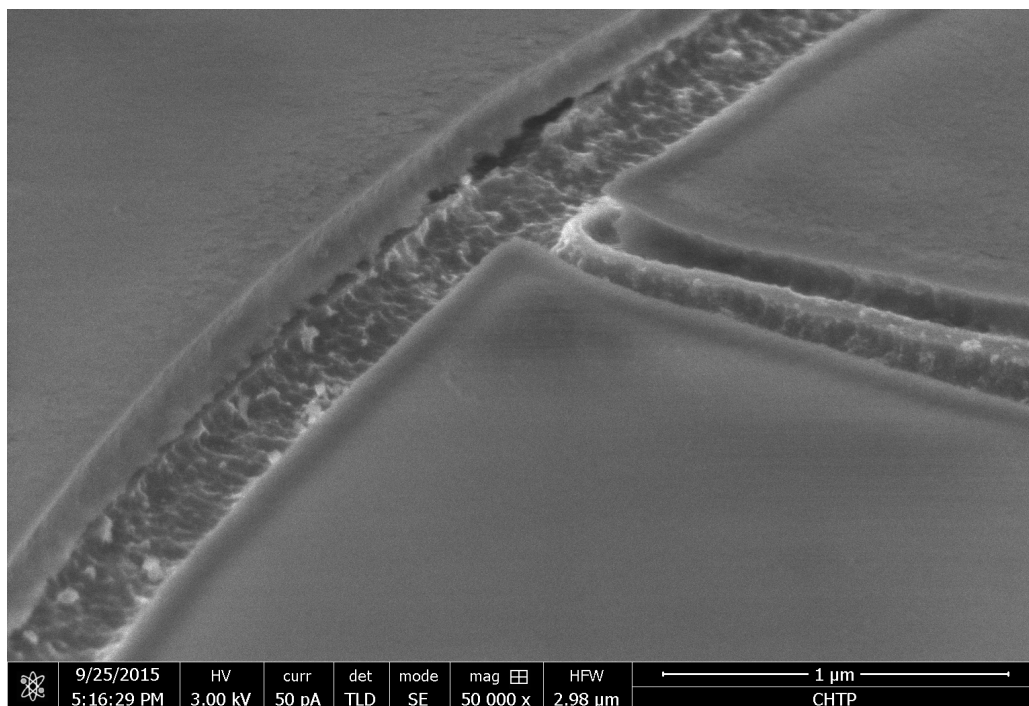


Figure S1. SEM image showing a *ca.* 175 nm thick Ni(OH)_x film obtained by photochemical decomposition of nickel (II) 2-ethylhexanoate spin-cast on a GC plate from a 0.2-M solution in hexanes.

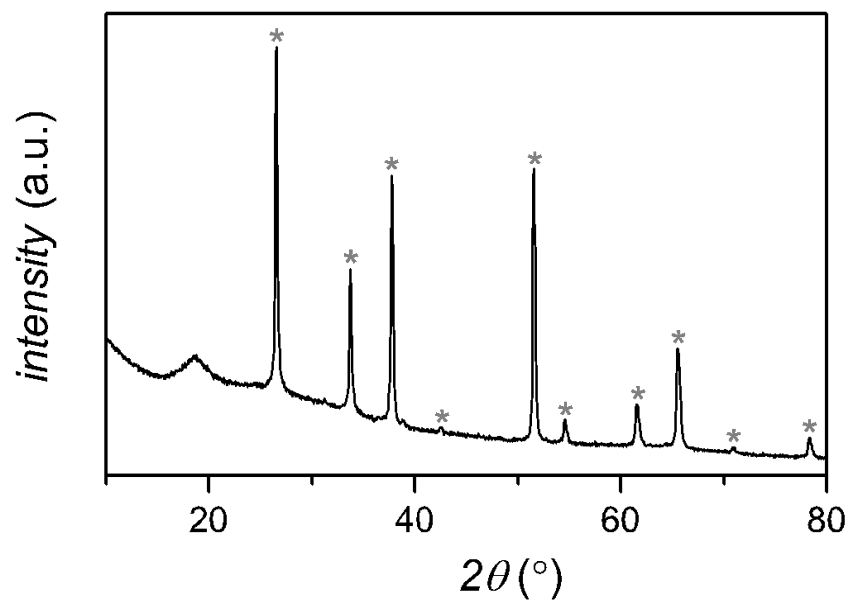


Figure S2. Powder X-ray diffraction pattern recorded on **Ni-fresh** produce a single, broad diffraction peak at 18.0° ($d = 4.8 \text{ \AA}$; reported (100) diffraction for $\alpha\text{-Ni(OH)}_2$ is 4.62 \AA). Stars correspond to reflections arising from FTO substrate.

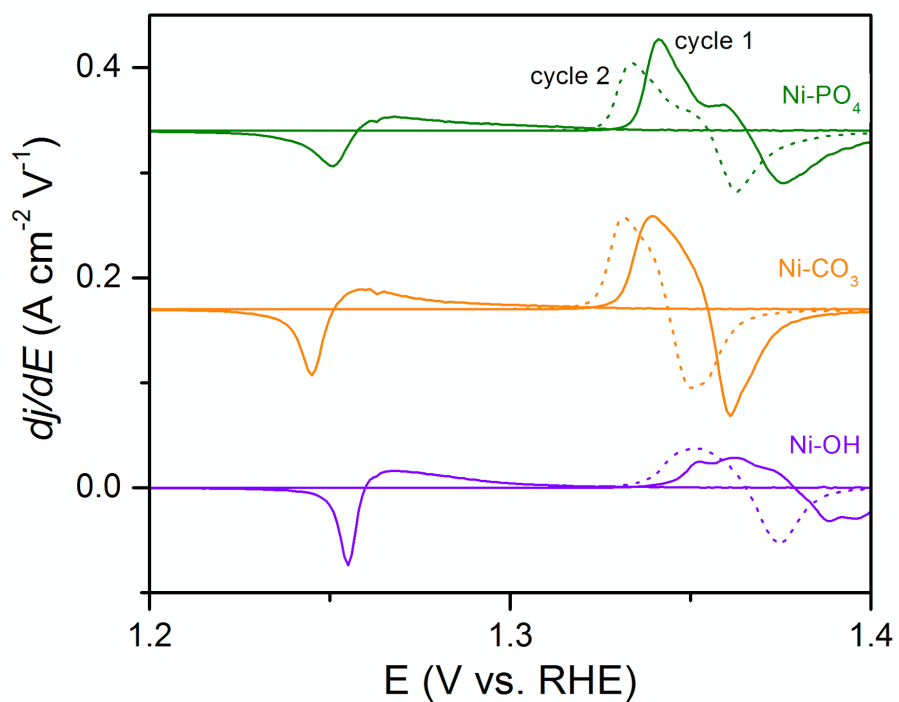


Figure S3. The first derivative of the CVs shown in Figure 3. The derivatives indicate that the redox peaks for **Ni-OH** are anodically shifted relative to **Ni-PO₄** and **Ni-CO₃** and exhibit a considerably more complex structure in the anodic peak.

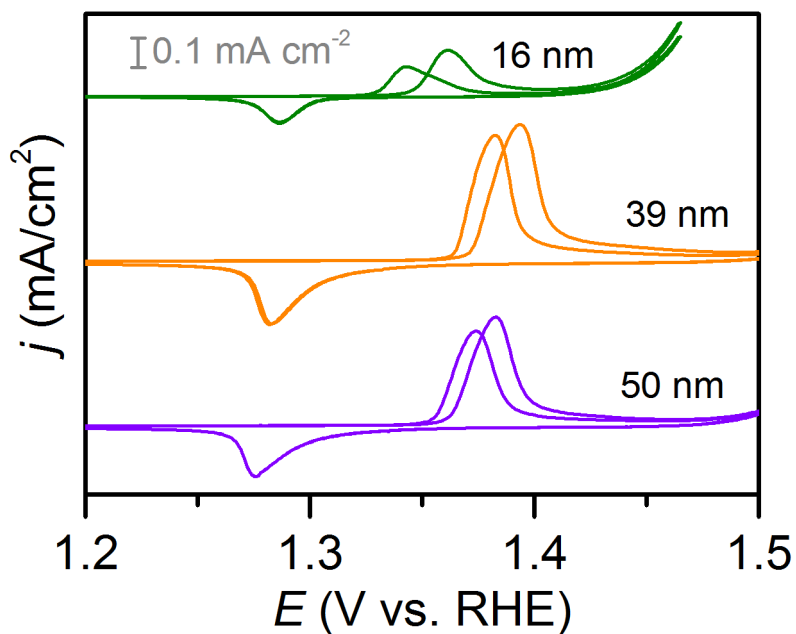


Figure S4. CVs acquired on Ni-cond films with varied film thickness at 1 mV s^{-1} . CVs shown correspond to the three thinnest films in Table 2. Experiments were performed at 1 mV s^{-1} in pH 14 electrolyte solutions.

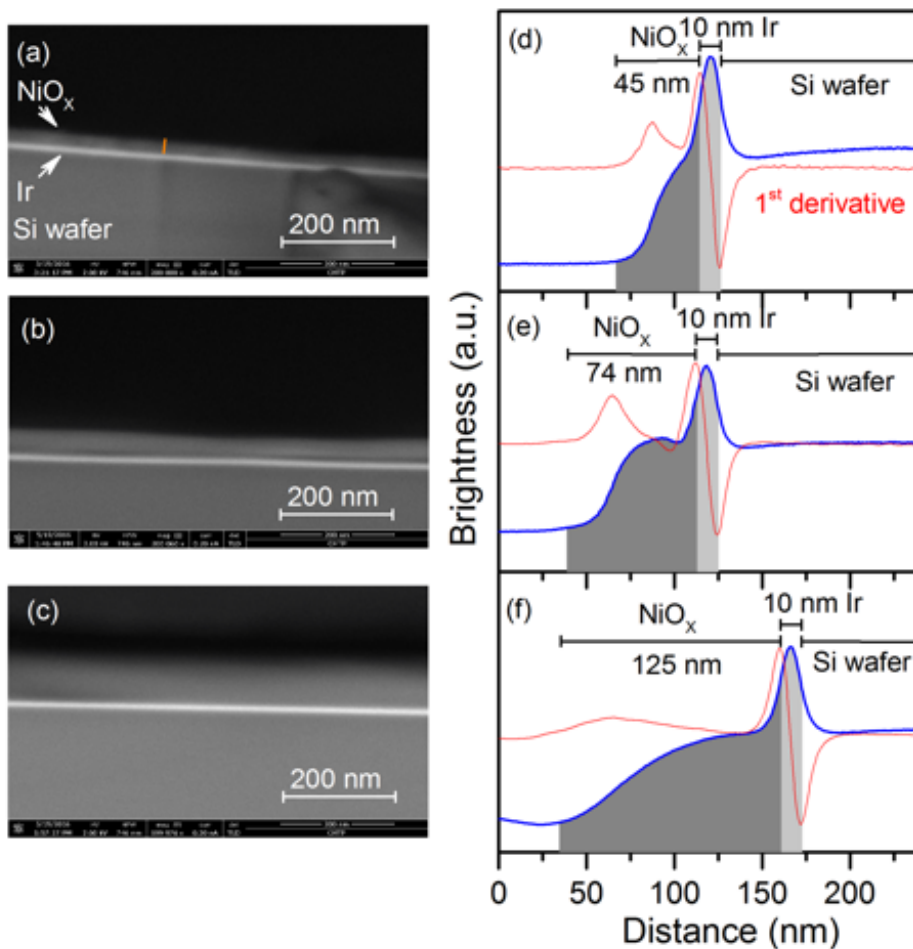


Figure S5. (a)-(c) Scanning electron microscopy was performed on a series of films fabricated with varied precursor solution concentrations to determine the relationship between the two parameters. (d)-(e) The thickness of each film was determined by cropping the SEM images to a 140 by 190 nm segment and analyzing the brightness profile perpendicular to the surface. The lower edge of the NiO_x surface was taken as the edge of the 10 nm iridium underlayer. The upper edge of NiO_x was taken from the first derivative of the brightness profile.

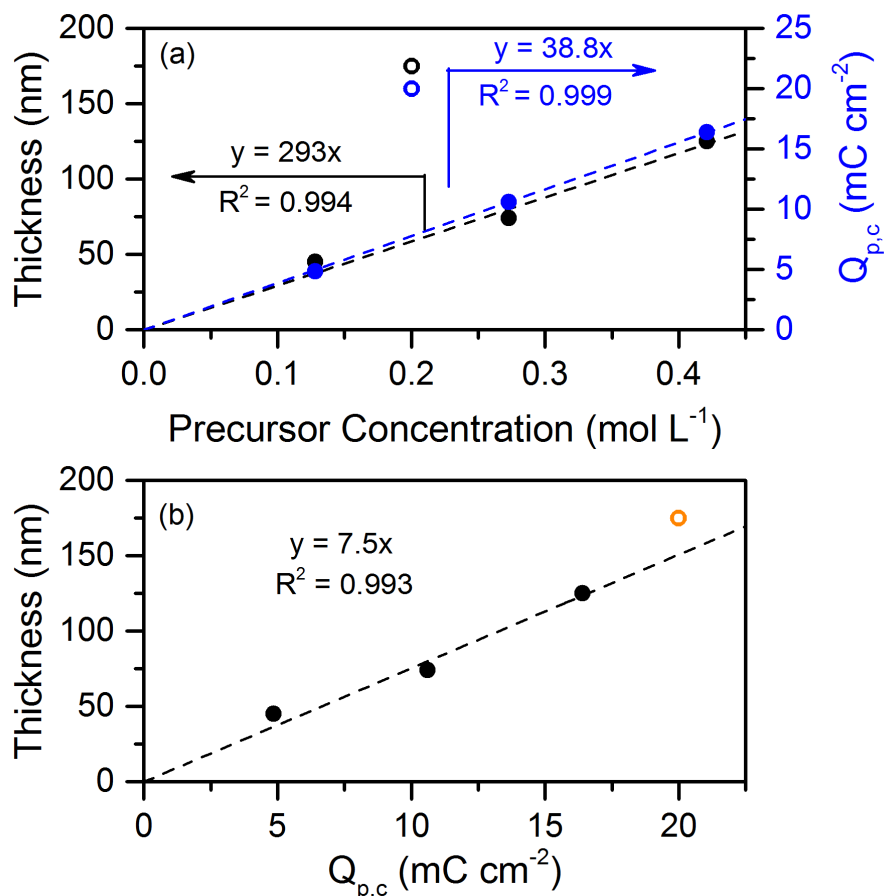


Figure S6. (a) The concentration of nickel (II) 2-ethylhexanoate in an isopropanol-based precursor solution linearly correlates to both film thickness (as measured in Figure S5) and the integrated charge below cathodic peak ($Q_{p,c}$) in CVs collected at 1 mV s⁻¹ on conditioned films. (b) The resultant linear correlation between $Q_{p,c}$ and film thickness was utilized to estimate the thickness of the rest of the films in the study. The hollow data points represent a NiO_x film deposited on glassy carbon from a 0.2 M solution in hexanes and were not considered in the linear fits. The hollow data points indicate that although the experimental protocol influences film thickness (e.g. substrate and solvent identity), the linear correlation between $Q_{p,c}$ and film thickness remains.

Table S1: Sample Parameters Used and the Resulting Diffusion Coefficients as Measured by Cyclic Voltammetry and the Potentiostatic Intermittent Titration Technique

Sample ^a	ΔQ^b / mC	A / cm ²	L / nm	D_{OH}^c / x 10 ⁻¹⁰ cm ² s ⁻¹	D_{OH}^d / x 10 ⁻¹⁰ cm ² s ⁻¹	D_{OH}^e / x 10 ⁻¹⁰ cm ² s ⁻¹
Ni-PO₄	13.9	0.35	225	3.2 (1.9)	1.4 (0.9)	1.9 (2.1)
Ni-CO₃	30.0	0.60	180	3.1 (1.8)	1.2 (0.9)	1.5 (2.1)
Ni-OH	64.8	1.05	150	1.3 (1.0)	0.7 (0.6)	0.8 (1.1)
Ni-cond	-	1.20	143	1.3 (1.1)	-	-

^a experiments were performed in triplicate, data for a single series of anodic and cathodic potential step experiments are shown; cathodic potential steps are shown in brackets

^b obtained from the intercept of anodic potential steps in Figure S6 using Eq. 3

^c semi-infinite diffusion using the Randles-Sevcik equation (Eq. 5); the slope of Figure S7

^d finite-space diffusion in the long-time domain (Eq. 3); the slope of Figure S8

^e semi-infinite diffusion in the short time domain (Eq. 4); the slope Figure S9

Table S2: Average Diffusion Coefficient Values as Measured by the Potentiostatic Intermittent Titration Technique and Cyclic Voltammetry

Sample ^a	D_{OH}^b / x 10 ⁻¹⁰ cm ² s ⁻¹	D_{OH}^c / x 10 ⁻¹⁰ cm ² s ⁻¹	D_{OH}^d / x 10 ⁻¹⁰ cm ² s ⁻¹	D_{OH}^e / x 10 ⁻¹⁰ cm ² s ⁻¹	τ / s
Ni-PO₄	3.2 (1.9)	1.4 ± 0.2 (0.92 ± 0.05)	1.7 ± 0.3 (2.1 ± 0.1)	2.1 ± 0.9 (1.7 ± 0.6)	2.6 (1.9)
Ni-CO₃	3.1 (1.8)	1.2 ± 0.1 (0.90 ± 0.05)	1.5 ± 0.1 (2.1 ± 0.1)	1.9 ± 0.9 (1.6 ± 0.6)	1.7 (1.4)
Ni-OH	1.3 (1.0)	0.70 ± 0.04 (0.55 ± 0.02)	0.80 ± 0.08 (1.1 ± 0.1)	0.93 ± 0.33 (0.90 ± 0.31)	2.5 (3.4)

^a average values from triplicate measurements; cathodic potential steps are shown in brackets

^b semi-infinite diffusion using the Randles-Sevcik equation (Eq. 5); the slope of Figure S7

^c finite-space diffusion in the long-time domain (Eq. 3); the slope of Figure S8

^d semi-infinite diffusion in the short time domain (Eq. 4); the peak of Figure S9

^e average D_{OH} all three techniques

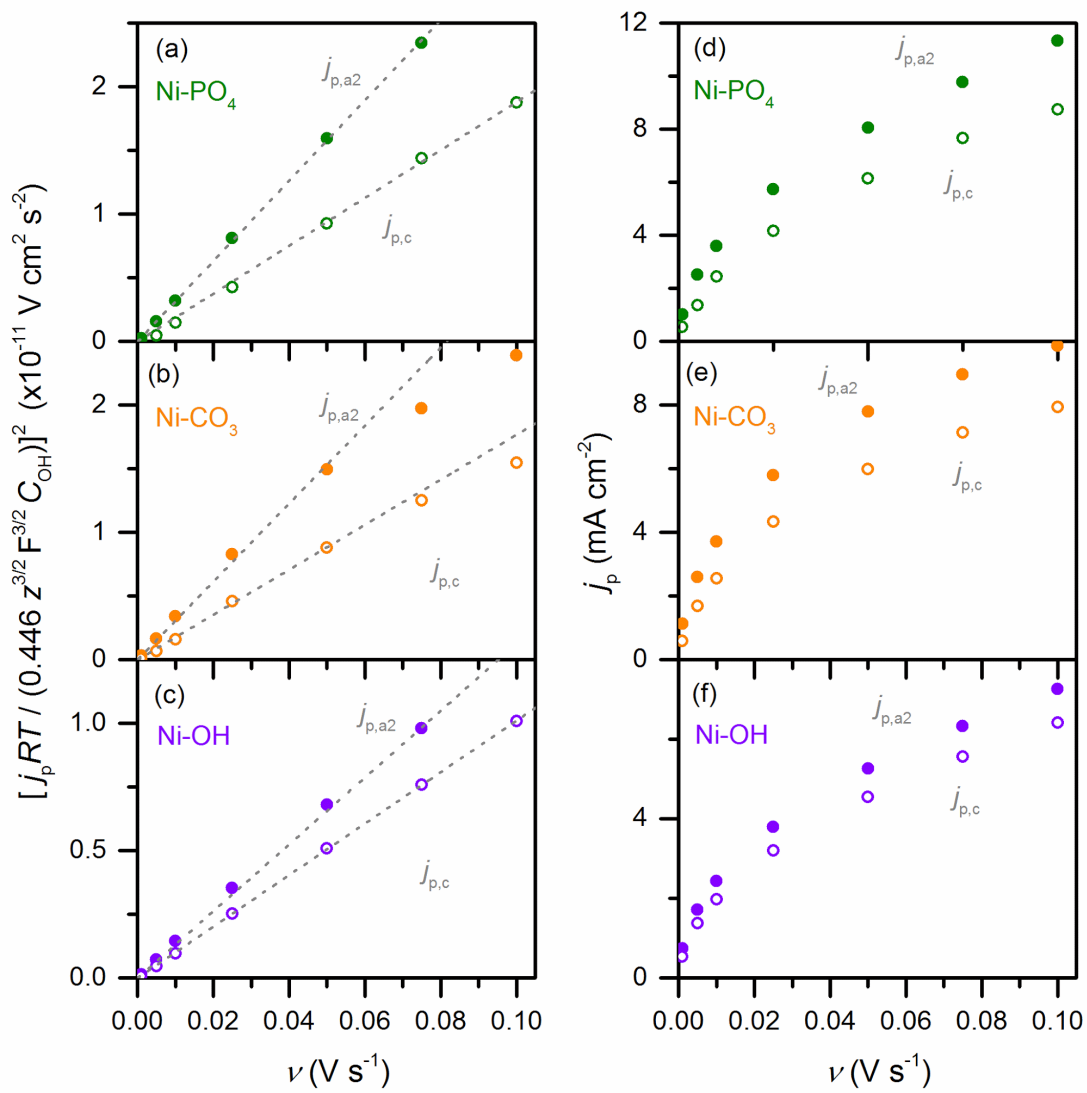


Figure S7. (a)-(c) Peak current density (j_p) was observed to be linearly correlated to $\nu^{1/2}$ for the stabilized anodic and cathodic peaks. Note that in order to facilitate direct comparisons the y-axes are normalized such that the linear slopes equal D_{OH} . The terms are defined in the main text. (d)-(f) A distinctly non-linear correlation was observed between ν and j_p .

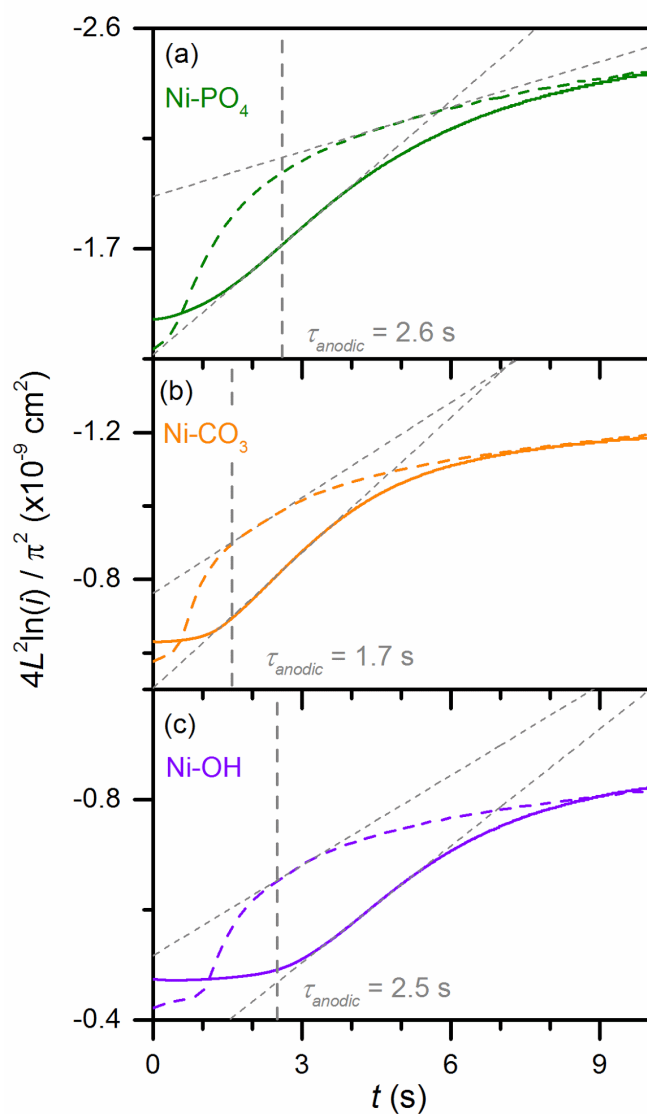


Figure S8. Sample of the chronoamperometric results for anodic potential steps (solid, colored lines) and cathodic potential steps (dashed, colored lines). The linear correlation between $\ln(i)$ and t for chronoamperometric experiments when $t > \tau$ (vertical dashed line) indicates the time domain where finite-space diffusion conditions exist (dashed gray lines). Note that the y-axis has been normalized such that the linear slope is equal to D_{OH} (see Eq. 3). Film thickness (L) values utilized are provided in Table S1; τ values shown were calculated from average D_{OH} values Table S2.

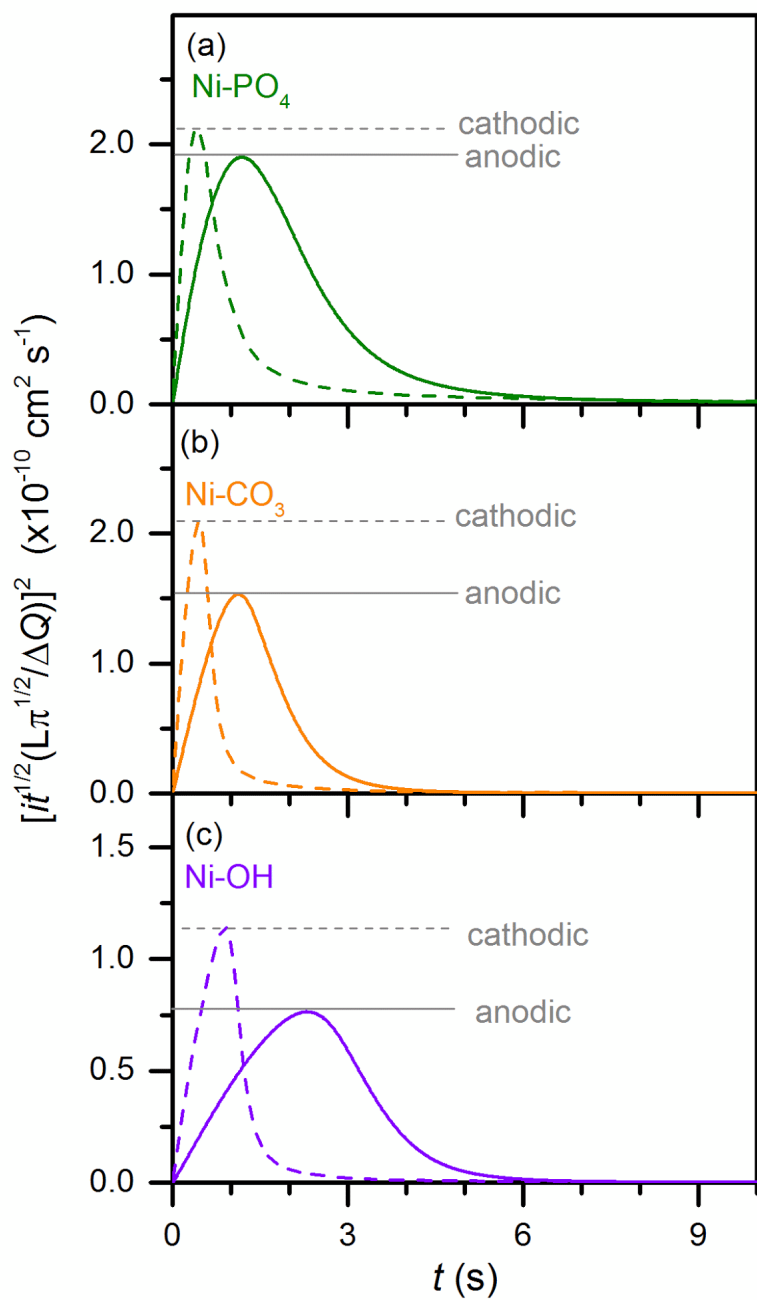


Figure S9. The peak observed in plots of $it^{1/2}(\Delta Q/L)$ vs. t are taken as the approximate D_{OH} . Note that the y-axis has been normalized such that the y-axes are equal to D_{OH} (see Eq. 4). Film thickness (L) and charge passed (ΔQ) values utilized in the normalization process are provided in Table S1.

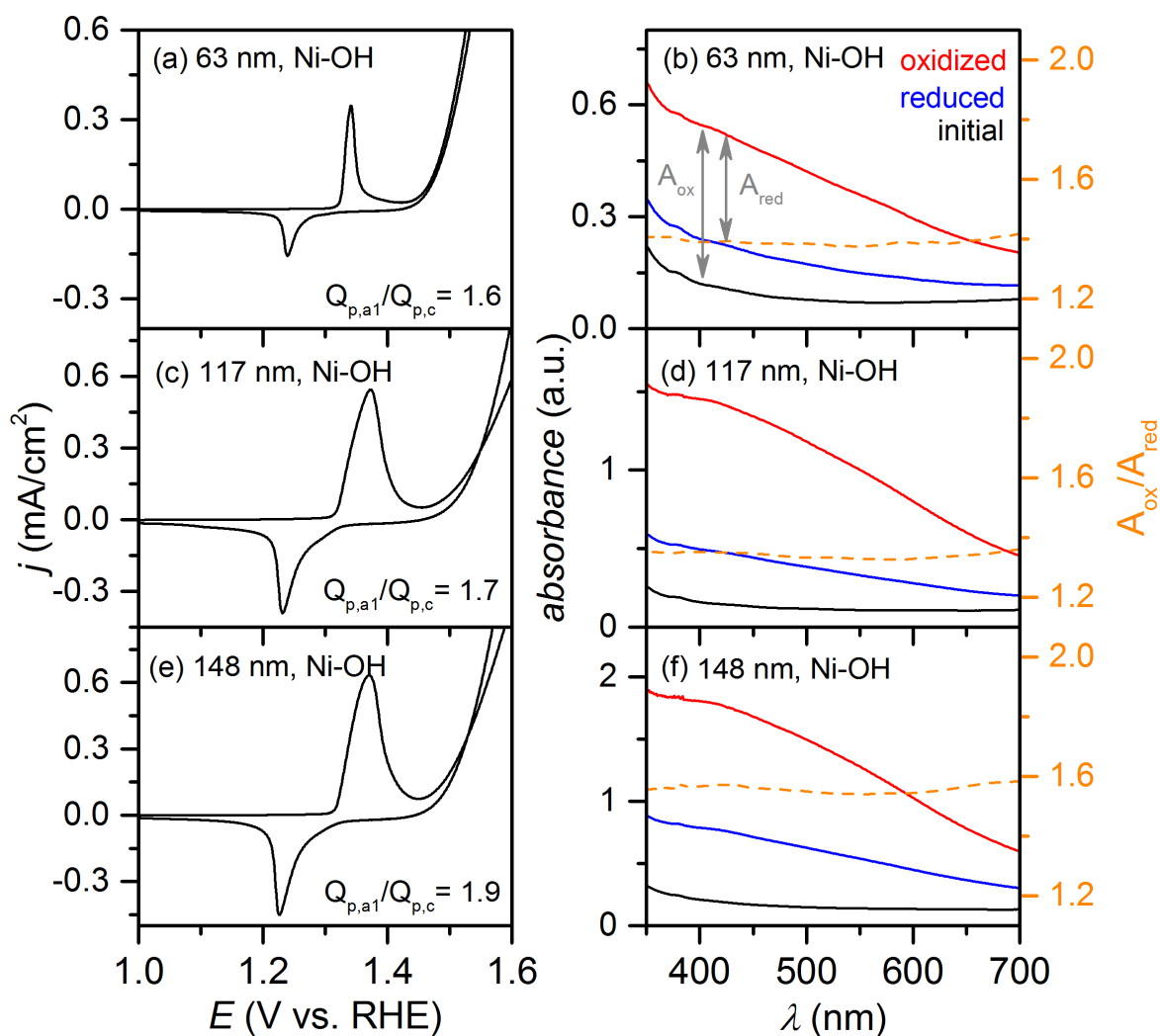


Figure S10. The degree of charge trapping in Ni-OH films with varied thickness was quantified by UV-visible spectroscopy. Spectra were recorded on the initial films (black line), after sweeping from 1.0 to 1.6 V vs. RHE (red line) and after subsequently sweeping from 1.6 to 1.0 V (blue line). The ratio of absorbance change upon oxidation to that on subsequent reduction ($A_{\text{ox}}/A_{\text{red}}$; dashed orange line) provides a measure of nickel sites trapped in an oxidized state.

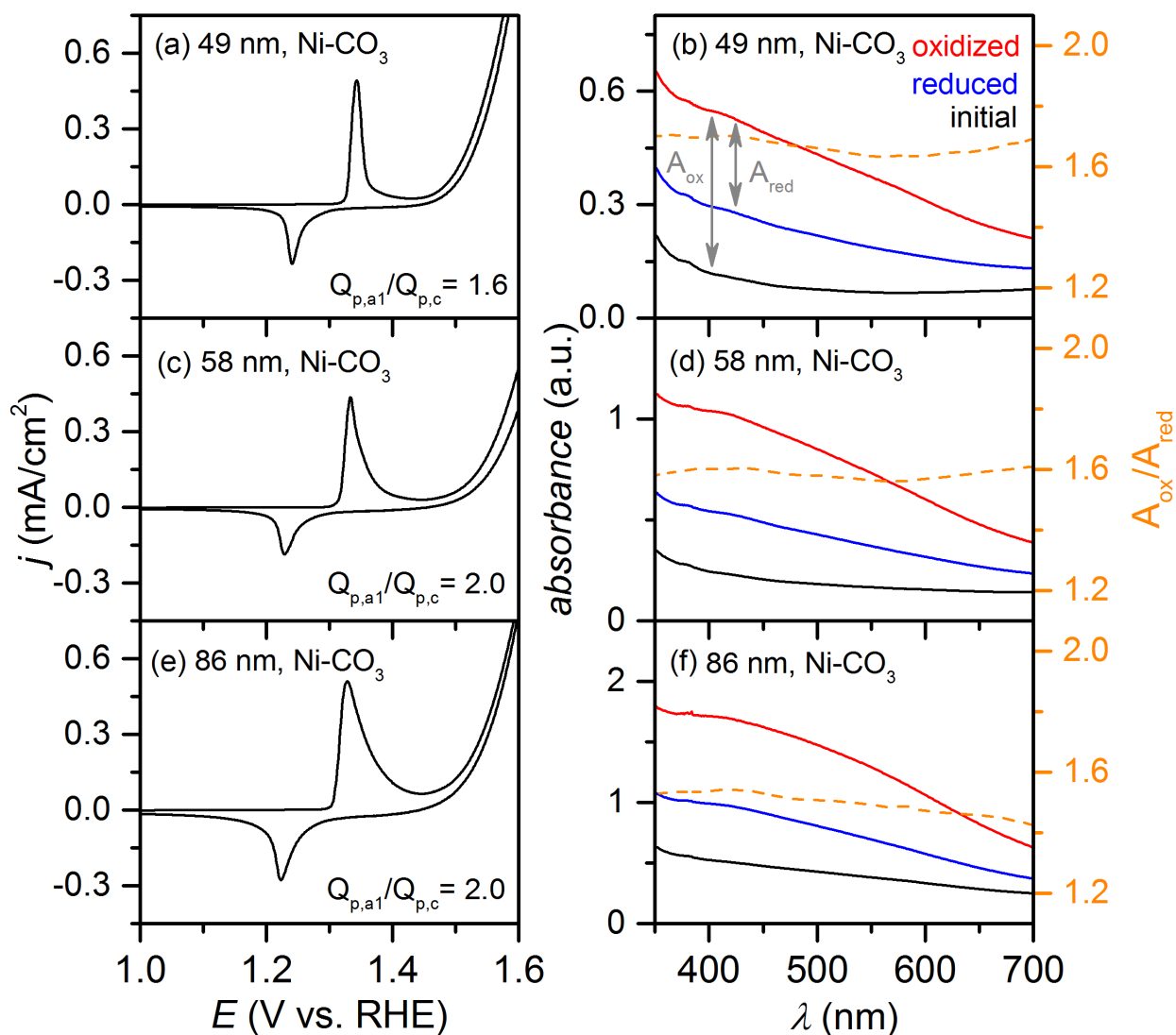


Figure S11. The degree of charge trapping in Ni-CO₃ films with varied thickness was quantified by UV-visible spectroscopy. Spectra were recorded on the initial films (black line), after sweeping from 1.0 to 1.6 V vs. RHE (red line) and after subsequently sweeping from 1.6 to 1.0 V (blue line). The ratio of absorbance change upon oxidation to that on subsequent reduction ($A_{\text{ox}}/A_{\text{red}}$; dashed orange line) provides a measure of nickel sites trapped in an oxidized state.

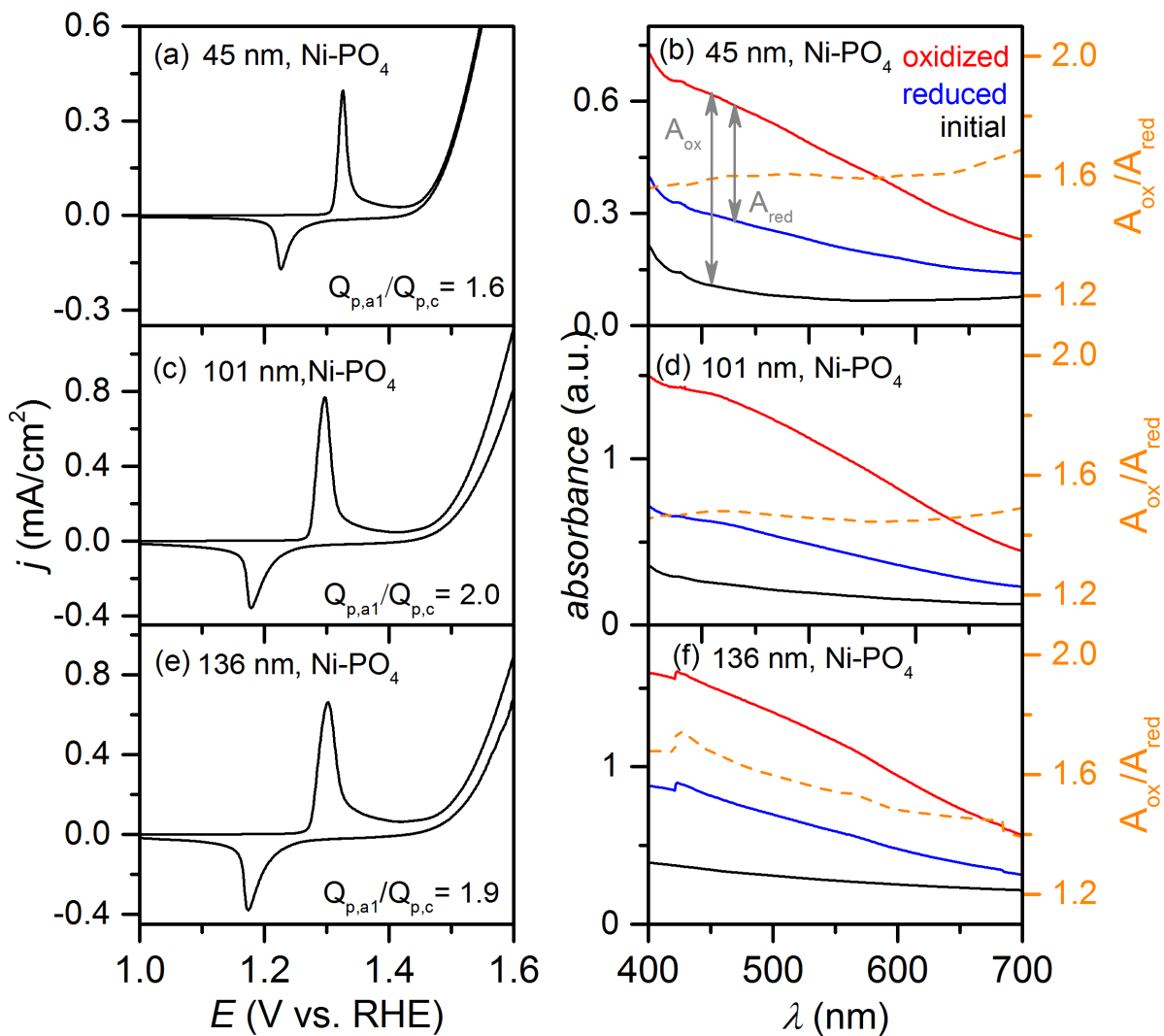


Figure S12. The degree of charge trapping in Ni-PO₄ films with varied thickness was quantified by UV-visible spectroscopy. Spectra were recorded on the initial films (black line), after sweeping from 1.0 to 1.6 V vs. RHE (red line) and after subsequently sweeping from 1.6 to 1.0 V (blue line). The ratio of absorbance change upon oxidation to that on subsequent reduction (A_{ox}/A_{red} ; dashed orange line) provides a measure of nickel sites trapped in an oxidized state.

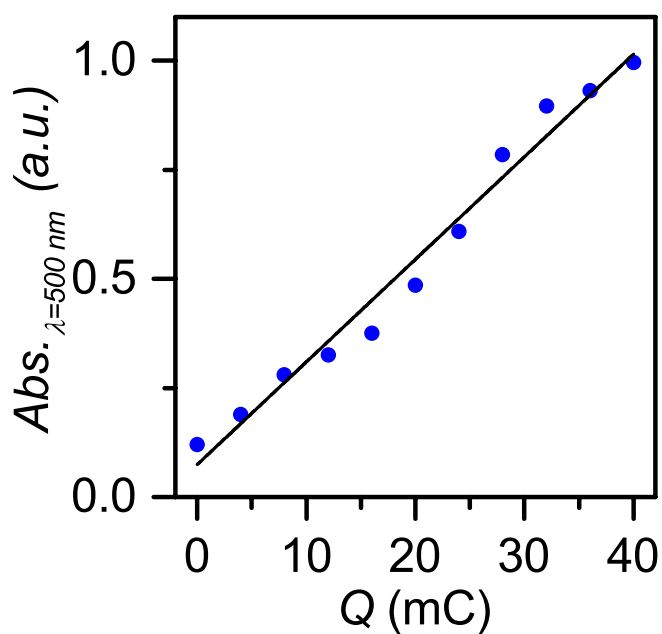
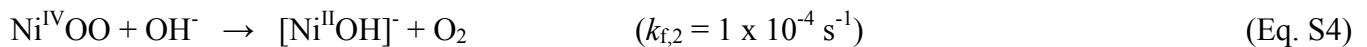
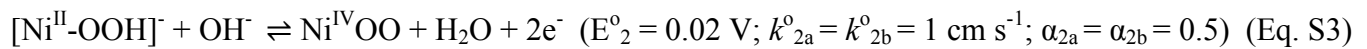
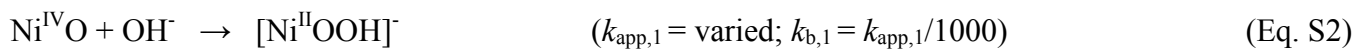


Figure S13. A linear correlation was observed between absorbance at 500 nm and anodic charge passed (Q) on a *ca.* 100 nm Ni-CO₃ film. Charge was passed in sequential 4 mC steps using a constant 1 mA current starting with a conditioned film until fully oxidized with *ex-situ* UV-visible measurements made during each step.

Digital Simulations of Voltammetric Behavior. Cyclic voltammetry simulations were performed using CH Instruments software package (Version 14.06), which utilizes the fast implicit finite difference algorithm.^{1,2} The reaction mechanism depicted in Figure 1 can be described as an $\mathbf{E}_1\mathbf{C}_1\mathbf{E}_2\mathbf{C}_2'$ mechanism, where \mathbf{E}_1 represents two one-electron transfer steps (E^{o1} in Figure 1), \mathbf{C}_1 is a chemical reaction between the oxidized product and OH^- ($k_{\text{app},1}$ in Figure 1), \mathbf{E}_2 is the second electron transfer process (E^{o2} in Figure 1), and \mathbf{C}_2' is the catalytic chemical step involving release of O_2 ($k_{\text{app},2}$ in Figure 1). Digital simulations were thus created using the mechanism laid out in Eqs. (S1) through (S4):



Simulation Strategy. A series of simulations were generated with a constant ν of 1 mV s^{-1} by systematically varying $k_{\text{app},1}$ from 0.00001 to 1.0 s^{-1} while holding the other parameters constant. Simulated CVs thereby reveal the expected differences in the voltammetric response for the $\mathbf{E}_1\mathbf{C}_1\mathbf{E}_2\mathbf{C}_2'$ reaction mechanism as a function of the rate of \mathbf{C}_1 . Under pseudo-1st order treatment ($k_{\text{app},1} = k_{f,1} a_{\text{OH}}$; see Eqs. (2) and (3) in main text) this behaviour should reflect behavioural changes induced by changes in a_{OH} within the NiO_x films. All nickel-containing species were modeled as surface-bound species.

Reaction Parameters. Experimental results suggest \mathbf{C}_1 can be considered to be chemically irreversible on the timescale of the CV experiments; the equilibrium constant for \mathbf{C}_1 was therefore maintained at $\log(K_1) = 3$ (*i.e.* $k_{b,1} = k_{\text{app},1}/1000$). Reactions \mathbf{E}_1 and \mathbf{E}_2 represent electron transfer reactions where major changes to the 2-dimensional $\text{Ni}(\text{OH})_2$ bonding structure are not believed to occur; both \mathbf{E}_1 and \mathbf{E}_2

were therefore assumed to be rapid ($k_{1a}^0 = k_{1b}^0 = k_{2a}^0 = k_{2b}^0 = 1 \text{ cm s}^{-1}$) and reversible ($\alpha_{1a} = \alpha_{1b} = \alpha_{2a} = \alpha_{2b} = 0.5$). The *ca.* 20 mV separation that is experimentally observed between $E_{p,a1}$ and $E_{p,a2}$ in CVs acquired at 1 mV s^{-1} was used as an estimate of the separation between $E^{o'1}$ and $E^{o'2}$ ($E_1^o = 0 \text{ V}$ and $E_2^o = 0.020 \text{ V}$; note that an arbitrary reference point of 0 V was employed for the simulations). The rate constant for C_2' ($k_{app,2}$) was experimentally measured (see below).

Model Generation. The response of the system was generalized using the dimensionless kinetic parameter, λ_1 , which is a function of scan rate (ν) and the sum of forward and reverse reaction rate constants ($k_{app,1} + k_{b,1}$):

$$\lambda_1 = \frac{RT(k_{app,1} + k_{b,1})}{F\nu} \quad (\text{Eq. S5})$$

As $\log(K_1) = 3$ in the model, contributions from $k_{b,1}$ are negligible and the equation simplifies to Eq. (8) in the main text. This equation highlights that the voltammetric behavior observed for the system will be affected by both $k_{app,1}$ and ν , with the two terms opposing each other.

Measurement of C_2' Reaction Kinetics. The initial report describing the experimental observation of the transfer of 4 electrons per nickel centre during initial oxidation of α -NiO_x identified a build-up of Ni^{IV}-OO on the electrode surface following oxidation.¹ An increase in steady state current (i_{ss}) measurements at $E_{p,a2}$ and detection of O₂ indicated that reaction C_2' acted as the rate-determining step for electrocatalytic OER. Two strategies were developed to exploit this behaviour and experimentally measure $k_{app,2}$, thereby improving the accuracy of simulated voltammetric behavior. In the first strategy the magnitude of steady state current increase (i_{ss}) was correlated to the amount of nickel on the electrode. In the second strategy the decay of an oxidized **Ni-cond** film was analyzed.

Strategy 1: An increase in steady state current was previously identified at potentials that correspond to $E_{p,a2}$ and interpreted as the accumulation of $\text{Ni}^{\text{IV}}\text{OO}$ on the surface of the electrode.³ These results are expanded on here by monitoring the magnitude of steady state current increase (taken as the difference between linear trend lines drawn before and after the current increase) upon variation of film thickness. Steady state current experiments were performed using a rotating ring-disc electrode (RRDE) on a series of anodically electrodeposited NiO_x films with varying thickness. Anodic electrodeposition was employed due to the inherent ability to control film thickness.⁴ An aqueous solution was prepared containing 0.1 M $\text{NaB}(\text{OH})_4$ and 0.4 mM $\text{Ni}(\text{NO}_3)_2$ in Fe-free H_2O (see main text). A total of 8 NiO_x films were anodically electrodeposited from this solution by applying +1.0 V vs. SSCE on a freshly cleaned glassy carbon disc until the desired charge density had passed. Steady state electrochemical measurements were then performed on each distinct NiO_x film (60-s intervals; 10 mV steps) while the RRDE electrode was rotated at 1500 RPM. The steady state electrocatalytic OER (i_{ss}) current due to $\text{Ni}^{\text{IV}}\text{OO}$ decay (Figure S14a) can be extracted from this data and described as:

$$\frac{i_{ss}}{n_{\text{OERFA}}} = k_{app,2} \Gamma_{\text{Ni}^{\text{IV}}\text{OO}} \quad (\text{Eq. S6})$$

Where n_{OER} is 4, the number of electrons transferred in the catalytic cycle. Considering the proposed mechanism (Figure 1) and the observation of a single cathodic peak in CV studies, the surface concentration of $\text{Ni}^{\text{IV}}\text{OO}$ ($\Gamma_{\text{Ni}^{\text{IV}}\text{OO}}$) can be determined by integration of the cathodic peak:

$$\Gamma_{\text{Ni}^{\text{IV}}\text{OO}} = \frac{Q_{p,c}}{n_{p,c}FA} \quad (\text{Eq. S7})$$

Where $n_{p,c}$ is the average number of electrons passed per nickel site; approximated as 1.7.^{3,5,6}

Substituting Eq. S6 into S7 and rearranging yields:

$$\frac{i_{ss}n_{p,c}}{n_{OER}} = k_{app,2}Q_{p,c} \quad (\text{Eq. S8})$$

The linear slope in a plot of $i_{ss} \cdot n_{p,c}/n_{OER}$ vs. $Q_{p,c}$ (Figure S14b) therefore provides an estimated $k_{app,2}$ of $7 \times 10^{-4} \text{ s}^{-1}$.

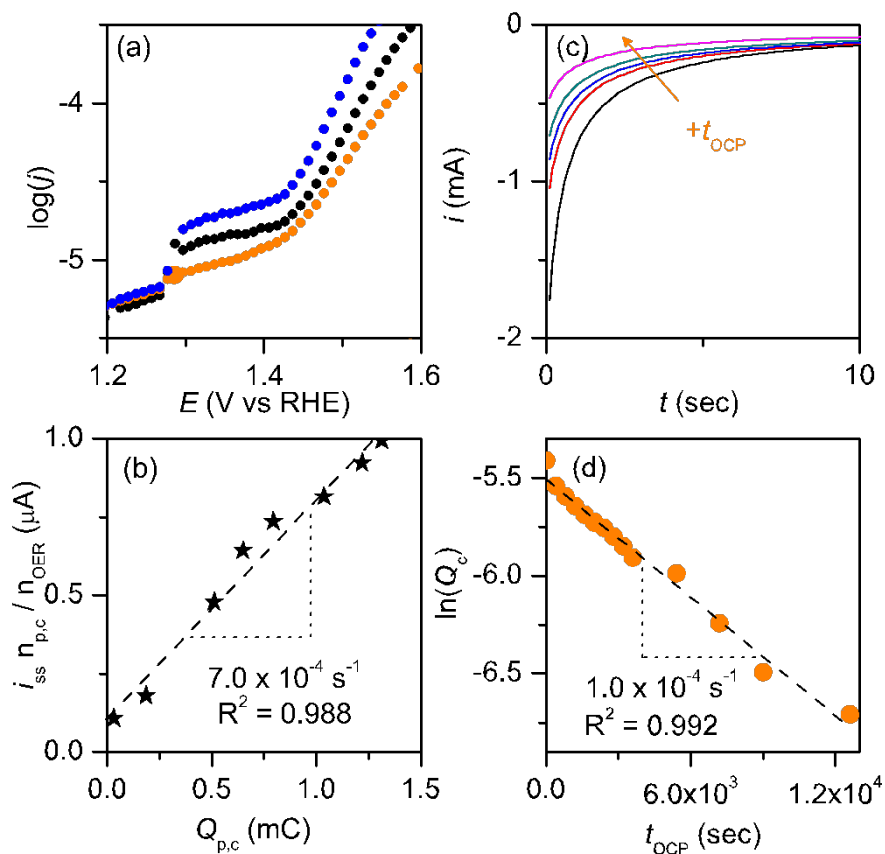


Figure S14. The chemical rate constant for reaction C'_2 ($k_{app,2}$) was experimentally measured using two different approaches. (a) The step-wise increase in steady-state current was dependent on thickness of NiO_x films. (b) The magnitude of this step (i_{ss}) varied linearly with the amount of nickel on the electrode surface, as approximated by $Q_{p,c}$, yielding an estimated rate constant of $7.0 \times 10^{-4} \text{ s}^{-1}$. Experiments were performed using a glassy carbon electrode with a surface area of 0.197 cm^2 . (c) An increase in the time that oxidized **Ni-cond** was allowed to decay at open-circuit potential (t_{OCP}) induced a decrease in the cathodic charge (Q_c) passed upon subsequent electrochemical reduction, as seen in chronoamperometric

traces. (d) A first-order kinetics plot of $\ln(Q_c)$ against t_{OCP} produced a linear plot with a slope of $1.0 \times 10^{-4} \text{ s}^{-1}$.

Strategy 2. A **Ni-cond** film on an Au substrate was subjected to a successive three-stage potential-step protocol: **(I)** conditioning of the film at 1.40 V vs. RHE for 60 s; **(II)** leaving the film to decay at open-circuit (E_{OC}) for variable periods of time (*vide infra*); and **(III)** applying a bias of 1.10 V to the film for 60 s. The anodic potential step at 1.40 V (**I**), which is sufficient to fully oxidize the film renders a stable current over the 60-s time period, thereby establishing a static concentration of the intermediate species immediately preceding the rate-determining step (RDS) in accordance with the steady-state approximation. The cathodic potential step (**III**) measures the amount of charge required to reduce the intermediate species present, where the concentration of intermediate decreases as the amount of time the cell is left to decay at E_{OC} increases (**II**). The three-stage potential-step experiment was repeated while progressively increasing the E_{OC} decay time in 400-s increments (**II**). The amount of charge passed during each cathodic potential step (Q_c) therefore provided a direct measure of the amount of intermediate species reduced at various points in the decay process, which, in turn, enabled application of classical chemical rate laws to study the decay of the oxidized intermediate species. The unambiguously linear relationship of $\ln(Q_c)$ versus *time* (Fig. S14) indicates that the decay process is first-order in the concentration of oxidized intermediate, with an approximate $k_{\text{app},2}$ of *ca.* $1.0 \times 10^{-4} \text{ s}^{-1}$ determined by the slope.

References:

- (1) Rudolph, M. A Fast Implicit Finite Difference Algorithm for the Digital Simulation of Electrochemical Processes. *J. Electroanal. Chem.* **1991**, *314*, 13–22.
- (2) Rudolph, M. Digital Simulations with the Fast Implicit Infinite Difference (FIFD) Algorithm Part II. an Improved Treatment of Electrochemical Mechanisms with Second-Order Reactions. *J. Electroanal. Chem.* **1992**, *338*, 85–98.
- (3) Smith, R. D. L.; Berlinguette, C. P. Accounting for the Dynamic Oxidative Behavior of Nickel Anodes. *J. Am. Chem. Soc.* **2016**, *138*, 1561–1567.
- (4) Dincă, M.; Surendranath, Y.; Nocera, D. G. Nickel-Borate Oxygen-Evolving Catalyst That Functions Under Benign Conditions. *Proc. Natl. Acad. Sci. U.S.A.* **2010**, *107*, 10337–10341.
- (5) Corrigan, D. A.; Knight, S. L. Electrochemical and Spectroscopic Evidence on the Participation of Quadrivalent Nickel in the Nickel Hydroxide Redox Reaction. *J. Electrochem. Soc.* **1989**, *136*, 613–619.
- (6) Bediako, D. K.; Lassalle-Kaiser, B.; Surendranath, Y.; Yano, J.; Yachandra, V. K.; Nocera, D. G. Structure-Activity Correlations in a Nickel-Borate Oxygen Evolution Catalyst. *J. Am. Chem. Soc.* **2012**, *134*, 6801–6809.